

NNP/MM: Accelerating molecular dynamics simulations with machine learning potentials and molecular mechanics

Raimondas Galvelis,^{*,†} Alejandro Varela-Rial,^{‡,¶} Stefan Doerr,[‡] Roberto Fino,[†]
Peter Eastman,[§] Thomas E. Markland,[§] John D. Chodera,^{||} and Gianni De
Fabritiis^{*,‡,¶,⊥}

[†]*Acellera Labs, C/ Doctor Trueta 183, 08005 Barcelona, Spain*

[‡]*Acellera Ltd, Devonshire House 582, HA7 1JS, United Kingdom*

[¶]*Computational Science Laboratory, Universitat Pompeu Fabra, PRBB, C/ Doctor
Aiguader 88, 08003 Barcelona, Spain*

[§]*Department of Chemistry, Stanford University, 337 Campus Drive, Stanford, CA, 94305,
USA*

^{||}*Computational and Systems Biology Program, Sloan Kettering Institute, Memorial Sloan
Kettering Cancer Center, New York, NY 10065, USA*

[⊥]*Institució Catalana de Recerca i Estudis Avançats (ICREA), Passeig Lluís Companys 23,
08010 Barcelona, Spain*

E-mail: r.galvelis@acellera.com; g.defabritiis@gmail.com

Abstract

Machine learning potentials have emerged as a means to enhance the accuracy of biomolecular simulations. However, their application is constrained by the significant computational cost arising from the vast number of parameters compared to traditional

molecular mechanics. To tackle this issue, we introduce an optimized implementation of the hybrid method (NNP/MM), which combines neural network potentials (NNP) and molecular mechanics (MM). This approach models a portion of the system, such as a small molecule, using NNP while employing MM for the remaining system to boost efficiency. By conducting molecular dynamics (MD) simulations on various protein-ligand complexes and metadynamics (MTD) simulations on a ligand, we showcase the capabilities of our implementation of NNP/MM. It has enabled us to increase the simulation speed by ~ 5 times and achieve a combined sampling of 1 μs for each complex, marking the longest simulations ever reported for this class of simulation.

Introduction

In the past decade, molecular dynamics (MD) has transitioned from CPU execution to accelerators such as graphical processing units (GPUs). Starting in 2006, CELLMD¹ and subsequently ACEMD² began leveraging GPUs to enhance biomolecular simulations. Numerous other MD codes have either adapted (e.g., AMBER,³ GROMACS,⁴ NAMD⁵) or been initially designed to utilize GPUs (e.g., OpenMM,⁶ HOOMD,⁷ TorchMD⁸). This innovation has improved the cost efficiency of MD simulations by two orders of magnitude.⁹

During the same timeframe, improvements in the accuracy of molecular mechanics (MM) and its force fields (FFs) have not advanced at a comparable pace as the simulation speed. Widely adopted biomolecular FFs, such as AMBER,^{10,11} CHARMM,^{12,13} and others, offer parameters for proteins and common biomolecules. However, obtaining accurate parameters for novel drug-like molecules remains a challenging task.¹⁴ The recent development of neural network potentials (NNPs) holds promise to address this issue.¹⁵ NNPs leverage the characteristic of neural networks (NNs) as *universal approximators*, which means they can approximate any function with arbitrary precision relative to the training data. In the context of molecular simulations, NNPs are designed to predict the energy and forces of quantum mechanics (QM) calculations.¹⁶

Recently, numerous NNPs have been proposed (SchNet,¹⁷ TensorMol,¹⁸ AIMNet,¹⁹ PhysNet,²⁰ DimeNet++,²¹ OrbNet,²² PaiNN,²³ SpookyNet,²⁴ NequIP,²⁵ OrbNet Denali,²⁶ TorchMD-NET,²⁷ MACE,²⁸ etc). One of the most used for organic molecules are ANI²⁹ and its derivatives³⁰⁻³³ based on a modified Behler-Parrinello (BP) symmetry function.³⁴ For example, the benchmarks of ANI-2x on a set of biaryl fragment, typically found in drug molecules, shows better accuracy than the established general small molecule FFs (CGenFF,^{35,36} GAFF,³⁷ OPLS,³⁸ and OpenFF³⁹). The mean absolute error for the entire potential energy profile and rotational barrier heights are 0.5 kcal/mol and 1.0 kcal/mol, respectively,⁴⁰ but it is orders of magnitude faster than its reference QM calculations at the DFT level (ω B97X/6-31G*).³³ However, the BP-type NNPs have several limitations. First, the long-range interactions are not properly accounted for. The NNPs only consider the chemical environment around each atom within a given cut-off distance (5.1 Å for ANI-2x). Second, a limited set of elements is supported (H, C, N, O, F, S, and Cl for ANI-2x). Finally, only neutral molecules can be computed.³³

Despite the current limitations, NNPs are already improving biomolecular simulations. It has demonstrated that the accuracy for drug-like molecules is improved¹⁴ by reparameterizing dihedral angles with ANI-1x.³⁰ Alternatively, the hybrid method of NNP and MM (NNP/MM)⁴¹ allows embedding NNP into a simulation. The main idea of NNP/MM is similar to QM/MM:⁴²⁻⁴⁴ an important region of a system is modeled with a more accurate method, while a less accurate and computationally cheaper one is used for the rest of the system.

Recently, Lahey and Rowley⁴¹ have demonstrated the first application of NNP/MM to protein-ligand complexes. NNP/MM is used to refine binding poses and to compute the conformational free energies. Rufa et al.⁴⁵ have computed the binding free energies of the Tyk2 congeneric ligand benchmark series⁴⁶ using alchemical free energy calculations. Instead of using NNP/MM directly, a non-equilibrium switching scheme has been devised to correct the standard MM calculations to NNP/MM accuracy. It reduces the errors from

1.0 kcal/mol to 0.5 kcal/mol. Vant et al.⁴⁷ have used NNP/MM for the refinement of a protein-ligand complex from cryo-electron microscopy data. The refinement with NNP/MM produces higher-quality models than QM/MM with the semi-empirical PM6 method at a lower computational cost. Xu et al.⁴⁸ have trained a specialized NNP for zinc and used NNP/MM to simulate zinc-containing proteins. The obtained results are in agreement with QM/MM calculations.

A critical limitation for the wider adoption of NNP/MM is the simulation speed. Despite NNP being much faster than QM, it is still slower than MM. For example, Lahey and Rowley⁴¹ and Vant et al.⁴⁷ have reported the simulations speed of 3.4 ns/day and 0.5 ns/day, respectively, on an NVIDIA TITAN Xp GPU. Also, the longest reported simulation is just 20 ns.⁴⁷

In this work, we present an optimized implementation of NNP/MM in ACEMD² based on OpenMM⁶ and PyTorch.⁴⁹ First, the method and relevant optimization strategies are introduced. Second, the capability of software is demonstrated by performing metadynamics (MTD)⁵⁰ simulations of a fragment of erlotinib and molecular dynamics (MD) simulations of four protein-ligand complexes. Finally, the installation and setup of simulations are shown.

Methods

In the NNP/MM approach, a system is partitioned into NNP and MM regions similarly to QM/MM.⁴²⁻⁴⁴ The total potential energy (V) consists of three terms:

$$V(\vec{r}) = V_{\text{NNP}}(\vec{r}_{\text{NNP}}) + V_{\text{MM}}(\vec{r}_{\text{MM}}) + V_{\text{NNP-MM}}(\vec{r}) \quad (1)$$

where V_{NNP} and V_{MM} are the potential energies of the NNP and MM regions, respectively. $V_{\text{NNP-MM}}$ is a coupling term; \vec{r} , \vec{r}_{NNP} , and \vec{r}_{MM} are the atomic position of the entire system, NNP region, and MM region, respectively.

It is required that the NNP potential (\vec{r}_{NNP}) is a function of the atomic position (\vec{r}_{NNP})

and atomic numbers (\vec{Z}_{NNP}) of the NNP region. The total charge (q_{NNP}) can be included if necessary:

$$V_{\text{NNP}}(\vec{r}_{\text{NNP}}) \equiv V_{\text{NNP}}(\vec{Z}_{\text{NNP}}, \vec{r}_{\text{NNP}}, q_{\text{NNP}}) \quad (2)$$

Also, it is required that V_{NNP} is differentiable with respect to \vec{r}_{NNP} to compute the atomic forces (\vec{F}_{NNP}):

$$\vec{F}_{\text{NNP}} = -\nabla V_{\text{NNP}} \quad (3)$$

In this work, we adapt the coupling term ($V_{\text{NNP-MM}}$) proposed by Lahey and Rowley:⁴¹

$$V_{\text{NNP-MM}}(\vec{r}) = \sum_i^{N_{\text{NNP}}} \sum_j^{N_{\text{MM}}} (V_C^{i,j} + V_{LJ}^{i,j}) \quad (4)$$

where $V_C^{i,j} = \frac{q_i q_j}{4\pi\epsilon_0 r_{ij}}$ is the Coulomb potential, $V_{LJ}^{i,j} = 4\epsilon_{ij} \left[\left(\frac{\sigma_{ij}}{r_{ij}} \right)^{12} - \left(\frac{\sigma_{ij}}{r_{ij}} \right)^6 \right]$ is the Lennard-Jones potential and N_{NNP} and N_{MM} are the number of NNP and MM atoms, respectively; q_i and q_j are the atomic charges; ϵ_{ij} and σ_{ij} are the Lennard-Jones parameters; r_{ij} is the distance between the atoms; and ϵ_0 is the vacuum permittivity (dielectric constant). In the context of QM/MM, this is known as the *mechanical embedding* scheme.^{43,44}

NNP/MM is implemented in ACEMD² using several software components. OpenMM,⁵¹ a GPU-accelerated MD library, is used to compute MM terms and propagate the MD trajectory. OpenMM-Torch,⁵² an OpenMM plugin, is used to compute the NNP term. It uses PyTorch,⁴⁹ a machine learning framework for NN training and inference on GPUs, to load and execute the NNP on GPU. TorchANI⁵³ is used to create the PyTorch model of ANI-2x.³³ NNPOps,⁵⁴ a library of optimized CUDA kernels for NNP, is used to accelerate critical parts of the computations. Future versions will integrate other NNPs available in TorchMD-NET.^{27,55}

We have optimized the performance of NNP/MM in three ways. First, all the terms of NNP and MM are computed on a GPU. Neither atomic positions nor atomic forces need to be transferred between the CPU and GPU, as is the case with the original implementation.⁴¹

Second, the featurizer of ANI has been implemented as a custom CUDA kernel and is available in the NNPOps library.⁵⁴ The original featurizer in TorchANI is implemented using only standard PyTorch operations, which are an inefficient way of performing this calculation. Third, the computation is parallelized over the NNs (ANI-2x has an ensemble of 8 NNs) and atoms taking advantage that the same molecule is computed repeatedly. The original implementation in TorchANI computes the NNs sequentially. The original TorchANI version is optimized for batch computing, i.e. many molecules are computed simultaneously, while for MD low-latency computing, i.e. one molecule is computed as fast as possible is necessary. The weights and biases of the atomic NNs are replicated and batched in the same order as the atoms in a molecule, allowing a GPU to efficiently parallelize the calculation for a single molecule. The implementation of the optimized NNs is available in the NNPOps library (<https://github.com/openmm/nnpops>).

Results and Discussion

Simulations of a fragment

We use metadynamics⁵⁰(MTD) to simulate a fragment (Figure 1) of erlotinib using two models: (1) the conventional MM with GAFF2³⁷ parameters for the fragment; and (2) the NNP/MM where the fragment is modeled with ANI-2x.³³ Lahey and Rowley⁴¹ reported that the fragment has a notable discrepancy between the potential energy surfaces of CGenFF³⁵ and ANI-1ccx.³¹ In this work, we expand the benchmark by computing the free energy surfaces.

We use the well-tempered MTD⁵⁶ with two dihedral angles (Figure 1) as collective variables. The MTD simulations use the NVT ensemble ($T = 310\text{K}$), the time step is set to 4.0fs for the MM simulations, and to 2.0fs for the NNP/MM simulations because they are unstable with 4.0fs. For MTD, PLUMED⁵⁷ is used. More details are provided in the supplementary information.

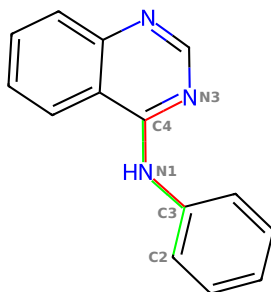


Figure 1: A fragment of erlotinib. The two dihedral angles used as the collective variable are shown in red and green.

The fragment was simulated for 100 ns with each method. This is sufficient to achieve extensive sampling in the collective variable space. The time series of the dihedral angles (Figure 1) are available in the supplementary information (Figure S1-S2).

The obtained free energy surfaces (Figure 2) show a significant difference between the models. The dominant conformer of the dihedral angle C3-N1-C4-N3 is predicted by GAFF2 and ANI-2x at $\sim 120^\circ$ and $\sim 0^\circ$, respectively. The fragment has two aromatic rings connected by a conjugated linker, so a planar conformation is expected to be energetically favorable. This is consistent with the potential energy surfaces reported by Lahey and Rowley (see Ref. 41, Figure 3b). Note, the fragment has been chosen for demonstration only and further analysis is beyond the scope of this work.

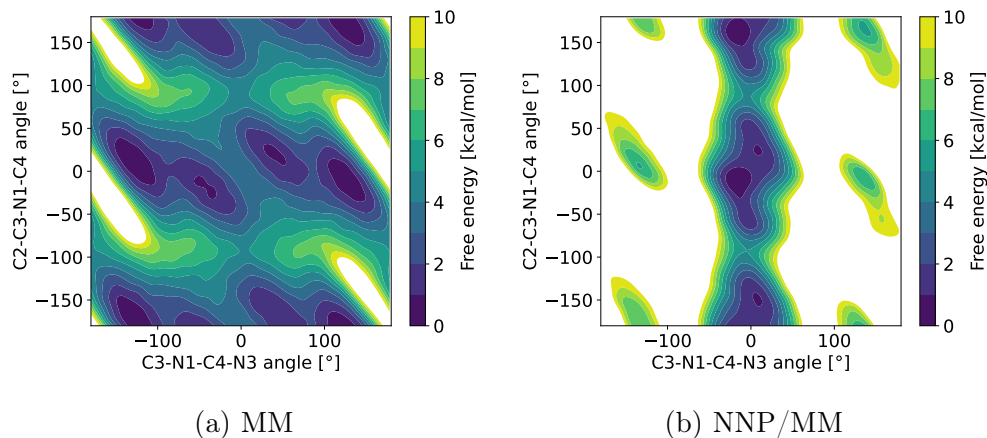


Figure 2: Free energy surface of a fragment (Figure 1) of erlotinib computed with MTD using two models MM (a) and NNP/MM (b).

Simulations of protein-ligand complexes

Protein-ligand complexes

We have selected four protein-ligand complexes from PDBbind-2019^{58,59} following these criteria. First, the ligand contains only elements supported by ANI-2x (H, C, N, O, F, S, and Cl)³³ and no charged functional groups (amine, carboxylate, etc). Second, the ligand has less than one hundred atoms. Third, the ligand has at least one rotatable bond, and the rotamers energies differ by >3 kcal/mol between GAFF2³⁷ and ANI-2x.³³ We use the *Parameterize* tool¹⁴ to detect the rotatable bond, scan the dihedral angles of rotatable bonds, and compute the relative rotamer energies. The summary of the protein-ligand complexes is given in Table 1 and the ligand structures are shown in Figure 3. Additionally, the energy profiles of the dihedral angle scan of the ligands are available in the supplementary information (Figure S2-S22).

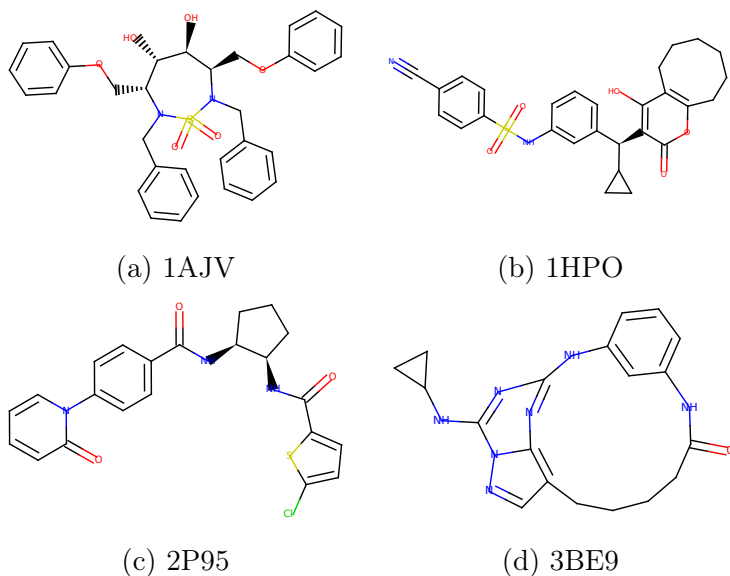


Figure 3: Ligand structures (a-d) of the selected protein-ligand complexes.

The protein-ligand complex preparation and equilibration have been carried out with HTMD.⁶⁴ Each complex has been simulated with two different methods: MM, where the ligand is parameterized with GAFF2³⁷ and NNP/MM, where the ligand is modeled with

Table 1: Summary of protein-ligand complexes.

System	Protein		Ligand		Total atoms
	atoms	residues	atoms	dihedrals	
1AJV ⁶⁰	3125	198	75	5	38325
1HPO ⁶¹	3133	198	64	6	47712
2P95 ⁶²	4398	286	50	7	52477
3BE9 ⁶³	5451	328	48	2	60412

ANI-2x.³³ The protein, in both cases, uses AMBER ff14SB¹¹ FF. The MD simulations use the NVT ensemble ($T = 310\text{ K}$), the time step is set to 4.0 fs for the MM simulations, and to 2.0 fs for the NNP/MM simulations because they are unstable with 4.0 fs. For each combination of a complex and method, 10 independent simulations of 100 ns are performed resulting in the combined sampling of 1 μs . More details are provided in the supplementary information.

Analysis of protein-ligand complexes

All the proteins and ligands maintain their structures in the simulations with both methods (MM and NNP/MM). The protein RMSD fluctuates in the range of 1.8-2.8 Å and the residue RMSF have similar magnitudes when comparing the same protein with both methods. The ligand RMSD fluctuates in the range of 0.2-1.7 Å. In the case of 1AJV and 2P95, there is no significant difference between MM and NNP/MM, but, in the case of 1HPO and 3BE9, the fluctuations are larger by $\sim 0.3\text{ Å}$ for NNP/MM. The time series of protein RMSD, residue RMSF, and ligand RMSD are available in the supplementary information (Figure S23-S34). The difference of the ligand RMSD is expected because, as previous works^{14,40,45} indicates, ANI-2x models the dihedral angles more accurately than GAFF. Also, it is important to note that our simulations are 50 times longer than previously reported⁴¹ and have not resulted in any non-physical conformation.

The dominant protein-ligand interactions (Figure 4) qualitatively agree between MM and NNP/MM for all the complexes. The full list of ligand-protein interactions and technical

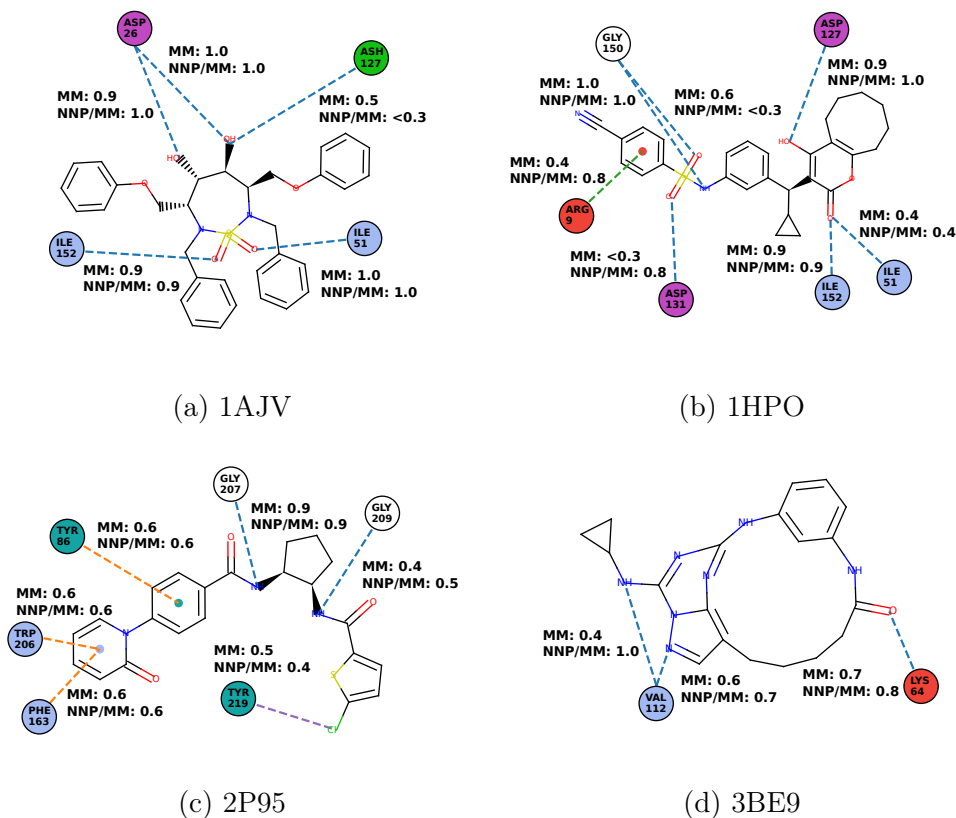


Figure 4: Probabilities of protein-ligand interactions for the different systems and methods (a-d). Protein residues are represented as disks (blue: non-polar, green: polar, red: positively charged, magenta: negatively charged, and dark cyan: aromatic). Interactions are depicted as dashed lines (blue: hydrogen bond, green: cation- π , orange: π - π interaction, and violet: σ -hole). The interactions with probabilities lower than 0.3 are excluded.

details are available in the supplementary information (Table S1-S8). Note, the protein-ligand systems have been chosen for demonstration only and further analysis is beyond the scope of this work.

Simulation speed

On average, NNPOps⁵⁴ accelerates ANI calculations (energy and forces) 6.5 times (Table 2). There is no strict dependency between the ligand size and the calculation time, which suggests significant overhead is coming from auxiliary operations rather than the computation of NNPs. The overhead mainly comes from PyTorch, which is optimized for batch computing rather than low latency.⁴⁹

Table 2: Comparison of ANI-2x inference (energy and forces) time (ms) using the original TorchANI and the TorchANI accelerated with NNPOps (TorchANI/NNPOps). The results were obtained with an NVIDIA RTX 4090 GPU.

System	TorchANI	TorchANI/NNPOps	Speed-up
1AJV	11.5	2.17	5.3
1HPO	11.3	1.91	5.9
2P95	13.0	1.54	8.4
3BE9	9.4	1.52	6.2
Average			6.5

Table 3: Comparison of MD simulation speed (ns/day) of NNP/MM using the original TorchANI, the TorchANI accelerated with NNPOps (TorchANI/NNPOps), and the TorchANI accelerated with NNPOps and just one model of ANI-2x (1 NN). For reference, MM speed is included. The results were obtained with an NVIDIA RTX 4090 GPU.

System	NNP/MM (TorchANI)*	NNP/MM (TorchANI/NNPOps)*	NNP/MM (1 NN)*	MM†
1AJV	12.6	60.1	155	1382
1HPO	13.4	65.9	152	1227
2P95	12.2	73.5	147	1006
3BE9	14.0	74.2	151	995

* 2 fs time step

† 4 fs time step

Overall NNP/MM is sped up 5.3 times (Table 3) on average when NNPOps⁵⁴ is used. Despite this improvement, NNP/MM is still about an order of magnitude slower than the conventional MM (Table 3), but further optimizations are possible. First, ANI-2x³³ uses an ensemble of 8 NNs. If only one NN could be used, the simulations would be 2.2 times faster on average (Table 3). Second, the time step for the NNP/MM simulations has to be reduced from 4 fs to 2 fs. If the constraint scheme could be adapted to allow 4 fs timestep, the simulations would be 2 times faster. Finally, not all the software components are already fully optimized. For example, the current implementation of OpenMM-Torch (<https://github.com/openmm/openmm-torch>) performs the NNP and MM calculations on a GPU sequentially, but it would be more efficient to do that concurrently.

Extensibility with other NNPs

Our implementation of NNP/MM is agnostic to the NNP model, i.e. it can use any model implemented with PyTorch. As a demonstration, we performed simulations with ANI-1x³⁰ and TorchMD-NET²⁷ trained with the ANI-1 data set.⁶⁵ The simulation speed benchmarks (Table 4) are available just for 3BE9 because both NNPs are limited to 4 elements (H, C, N, and O).

Table 4: Comparison of MD simulation speed of ANI-1x and TorchMD-NET and their accuracy in mean absolute error (MAE). The results were obtained with an NVIDIA RTX 4090 GPU.

System 3BE9	ANI-1x*	TorchMD-NET*
speed (ns/day)	127	17.0
accuracy (eV)	0.057	0.010

* 2 fs time step

Software installation and usage

ACEMD can be installed with the Conda package management system.⁶⁶ For dependencies, Conda-forge⁶⁷ is used to ensure compatibility with all major Linux distributions (refer to the ACEMD documentation for details at <https://software.acellera.com>). The installation command:

```
$ conda install -c conda-forge \  
    -c acellera \  
    -c acellera/label/rc \  
    acemd=4
```

For the best performance, it is recommended to have an NVIDIA GPU and its latest drivers installed, but it is possible to run on a CPU only.

The setup of an NNP/MM simulation consists of the following steps. First, a system needs to be prepared for a conventional MM simulation (i.e. initial structure, topology, and force field parameters). Note that the NNP atoms need to be assigned partial charges and Lennard-Jones parameters to compute the coupling term correctly. The system preparation can be easily accomplished with HTMD.^{64,68} Second, NNP model files need to be generated with `prepare-nnp` tool included with ACEMD. It needs the initial structure (e.g. `structure.pdb`), a selection of the NNP atoms (e.g. `"resname MOL"`), and a name of NNP

```
$ prepare-nnp structure.pdb --selection "resname MOL" \  
--model ANI-2x
```

The tool generates several files including `model.json`. Currently, we plan to support the NNP models from TorchANI⁵³ and TorchMD-NET²⁷ but other models will also be supported in the future. Finally, an ACEMD input file needs to be prepared as for a conventional MD simulation (refer to the ACEMD documentation⁶⁹ for details) and needs just one additional line (`nnpfile model.json`) to enable NNP/MM.

Conclusion

We have showcased an optimized implementation of NNP/MM in ACEMD,² based on OpenMM⁶ and PyTorch,⁴⁹ which delivers simulation speeds of approximately 5 times faster than previously reported. While still slower than classical force fields, the enhanced accuracy of NNPs may justify the increased computational expense (see Rufa et al.⁴⁵). We anticipate this performance gap will continue to shrink in the future. Presently, NNPs have limited applicability due to constraints on charges and elements, but improvements are expected in the near future.

We validated our implementation by conducting metadynamics simulations of an erlotinib fragment and molecular dynamics simulations of four protein-ligand complexes. The fragment simulation results are consistent with prior findings, while the complex simulations

exceeded previous durations by over an order of magnitude. These outcomes confirm the effectiveness of our implementation and demonstrate its practical application. Furthermore, NNP/MM can be combined with the enhanced sampling methods (e.g. metadynamics,⁵⁰ replica exchange,⁷⁰ steered molecular dynamics,⁷¹ etc.) and it holds significant potential for alchemical free energy simulations.⁴⁵ It is particularly beneficial for drug discovery efforts, where the simulation of novel molecules is routine but accurate force field parameters may be lacking.

Acknowledgement

The authors thank the volunteers of GPUGRID.net for donating computing time. This project has received funding from the Torres-Quevedo Programme from the Spanish National Agency for Research (PTQ-17-09078 / AEI / 10.13039/501100011033) (RG); the European Union’s Horizon 2020 research and innovation programme under grant agreement No. 823712 (RG, AV, RF); the Industrial Doctorates Plan of the Secretariat of Universities and Research of the Department of Economy and Knowledge of the Generalitat of Catalonia (AV); the Chan Zuckerberg Initiative DAF (grant number: 2020-219414), an advised fund of Silicon Valley Community Foundation (SD, PE); and the project PID2020-116564GB-I00 has been funded by MCIN / AEI / 10.13039/501100011033. Research reported in this publication was supported by the National Institute of General Medical Sciences (NIGMS) of the National Institutes of Health under award number GM140090 (PE, TEM, JDC, GDF). The content is solely the responsibility of the authors and does not necessarily represent the official views of the National Institutes of Health. JDC is a current member of the Scientific Advisory Board of OpenEye Scientific Software, Redesign Science, Ventus Therapeutics, and Interline Therapeutics, and has equity interests in Redesign Science and Interline Therapeutics. The Chodera laboratory receives or has received funding from multiple sources, including the National Institutes of Health, the National Science Foundation, the Parker Institute

for Cancer Immunotherapy, Relay Therapeutics, Entasis Therapeutics, Silicon Therapeutics, EMD Serono (Merck KGaA), AstraZeneca, Vir Biotechnology, Bayer, XtalPi, Interline Therapeutics, the Molecular Sciences Software Institute, the Starr Cancer Consortium, the Open Force Field Consortium, Cycle for Survival, a Louis V. Gerstner Young Investigator Award, and the Sloan Kettering Institute. A complete funding history for the Chodera lab can be found at <http://choderalab.org/funding>.

Supporting Information Available

The following files are available free of charge:

- SI.pdf: the time series of the dihedral angles of the fragment; the energy profiles of the dihedral angle scan of the ligands; the protein and ligand RMSD and residue RMSF for all the simulations; and the full list of ligand-protein interactions.

Installation instructions for the software are available at <https://software.acellera.com>.

References

- (1) De Fabritiis, G. Performance of the Cell processor for biomolecular simulations. *Comput. Phys. Commun* **2007**, *176*, 660–664.
- (2) Harvey, M. J.; Giupponi, G.; Fabritiis, G. D. ACEMD: accelerating biomolecular dynamics in the microsecond time scale. *J. Chem. Theory Comput* **2009**, *5*, 1632–1639.
- (3) Salomon-Ferrer, R.; Case, D. A.; Walker, R. C. An overview of the Amber biomolecular simulation package. *Wiley Interdiscip. Rev. Comput. Mol. Sci* **2013**, *3*, 198–210.
- (4) Abraham, M. J.; Murtola, T.; Schulz, R.; Páll, S.; Smith, J. C.; Hess, B.; Lindahl, E. GROMACS: High performance molecular simulations through multi-level parallelism from laptops to supercomputers. *SoftwareX* **2015**, *1*, 19–25.

- (5) Phillips, J. C.; Hardy, D. J.; Maia, J. D.; Stone, J. E.; Ribeiro, J. V.; Bernardi, R. C.; Buch, R.; Fiorin, G.; Hénin, J.; Jiang, W.; McGreevy, R.; Melo, M. C. R.; Radak, B. K.; Skeel, R. D.; Singharoy, A.; Wang, Y.; Roux, B.; Aksimentiev, A.; Luthey-Schulten, Z.; Kalé, L. V.; Schulten, K.; Chipot, C.; Tajkhorshid, E. Scalable molecular dynamics on CPU and GPU architectures with NAMD. *J. Chem. Phys* **2020**, *153*, 044130.
- (6) Eastman, P.; Pande, V. OpenMM: A hardware-independent framework for molecular simulations. *Comput. Sci. Eng* **2010**, *12*, 34–39.
- (7) Anderson, J.; Keys, A.; Phillips, C.; Dac Nguyen, T.; Glotzer, S. HOOMD-blue, general-purpose many-body dynamics on the GPU. APS March Meeting Abstracts. 2010; pp Z18–008.
- (8) Doerr, S.; Majewski, M.; Pérez, A.; Krämer, A.; Clementi, C.; Noe, F.; Giorgino, T.; De Fabritiis, G. Torchmd: A deep learning framework for molecular simulations. *J. Chem. Theory Comput* **2021**, *17*, 2355–2363.
- (9) Stone, J. E.; Hardy, D. J.; Ufimtsev, I. S.; Schulten, K. GPU-accelerated molecular modeling coming of age. *J. Mol. Graph. Model* **2010**, *29*, 116–125.
- (10) Cornell, W. D.; Cieplak, P.; Bayly, C. I.; Gould, I. R.; Merz, K. M.; Ferguson, D. M.; Spellmeyer, D. C.; Fox, T.; Caldwell, J. W.; Kollman, P. A. A Second Generation Force Field for the Simulation of Proteins, Nucleic Acids, and Organic Molecules. *J. Am. Chem. Soc* **1995**, *117*, 5179–5197.
- (11) Maier, J. A.; Martinez, C.; Kasavajhala, K.; Wickstrom, L.; Hauser, K. E.; Simmerling, C. ff14SB: improving the accuracy of protein side chain and backbone parameters from ff99SB. *J. Chem. Theory Comput* **2015**, *11*, 3696–3713.
- (12) MacKerell, A. D.; Bashford, D.; Bellott, M.; Dunbrack, R. L.; Evanseck, J. D.; Field, M. J.; Fischer, S.; Gao, J.; Guo, H.; Ha, S.; Joseph-McCarthy, D.; Kuchnir, L.;

- Kuczera, K.; Lau, F. T. K.; Mattos, C.; Michnick, S.; Ngo, T.; Nguyen, D. T.; Prodrom, B.; Reiher, W. E.; Roux, B.; Schlenkrich, M.; Smith, J. C.; Stote, R.; Straub, J.; Watanabe, M.; Wiórkiewicz-Kuczera, J.; Yin, D.; Karplus, M. All-Atom Empirical Potential for Molecular Modeling and Dynamics Studies of Proteins. *J. Phys. Chem. B* **1998**, *102*, 3586–3616.
- (13) Huang, J.; MacKerell Jr, A. D. CHARMM36 All-Atom Additive Protein Force Field: Validation Based on Comparison to NMR Data. *J. Comput. Chem* **2013**, *34*, 2135–2145.
- (14) Galvelis, R.; Doerr, S.; Damas, J. M.; Harvey, M. J.; De Fabritiis, G. A Scalable Molecular Force Field Parameterization Method Based on Density Functional Theory and Quantum-Level Machine Learning. *J. Chem. Inf. Model* **2019**, *59*, 3485–3493.
- (15) Noé, F.; Tkatchenko, A.; Müller, K.-R.; Clementi, C. Machine learning for molecular simulation. *Annu. Rev. Phys. Chem* **2020**, *71*, 361–390.
- (16) Behler, J. Constructing high-dimensional neural network potentials: A tutorial review. *Int. J. Quantum Chem* **2015**, *115*, 1032–1050.
- (17) Schütt, K. T.; Sauceda, H. E.; Kindermans, P.-J.; Tkatchenko, A.; Müller, K.-R. SchNet—A deep learning architecture for molecules and materials. *J. Chem. Phys* **2018**, *148*, 241722.
- (18) Yao, K.; Herr, J. E.; Toth, D. W.; Mckintyre, R.; Parkhill, J. The TensorMol-0.1 model chemistry: a neural network augmented with long-range physics. *Chem. Sci* **2018**, *9*, 2261–2269.
- (19) Zubatyuk, R.; Smith, J. S.; Leszczynski, J.; Isayev, O. Accurate and transferable multi-task prediction of chemical properties with an atoms-in-molecules neural network. *Sci. Adv* **2019**, *5*, eaav6490.

- (20) Unke, O. T.; Meuwly, M. PhysNet: A neural network for predicting energies, forces, dipole moments, and partial charges. *J. Chem. Theory Comput* **2019**, *15*, 3678–3693.
- (21) Klicpera, J.; Giri, S.; Margraf, J. T.; Günnemann, S. Fast and Uncertainty-Aware Directional Message Passing for Non-Equilibrium Molecules. *arXiv preprint arXiv:2011.14115* **2020**,
- (22) Qiao, Z.; Welborn, M.; Anandkumar, A.; Manby, F. R.; Miller III, T. F. OrbNet: Deep learning for quantum chemistry using symmetry-adapted atomic-orbital features. *J. Chem. Phys* **2020**, *153*, 124111.
- (23) Schütt, K.; Unke, O.; Gastegger, M. Equivariant message passing for the prediction of tensorial properties and molecular spectra. International Conference on Machine Learning. 2021; pp 9377–9388.
- (24) Unke, O. T.; Chmiela, S.; Gastegger, M.; Schütt, K. T.; Sauceda, H. E.; Müller, K.-R. SpookyNet: Learning force fields with electronic degrees of freedom and nonlocal effects. *Nat. Commun* **2021**, *12*, 7273.
- (25) Batzner, S.; Smidt, T. E.; Sun, L.; Mailoa, J. P.; Kornbluth, M.; Molinari, N.; Kozinsky, B. SE(3)-equivariant graph neural networks for data-efficient and accurate interatomic potentials. *arXiv preprint arXiv:2101.03164* **2021**,
- (26) Christensen, A. S.; Sirumalla, S. K.; Qiao, Z.; O’Connor, M. B.; Smith, D. G.; Ding, F.; Bygrave, P. J.; Anandkumar, A.; Welborn, M.; Manby, F. R.; Miller III, T. F. OrbNet Denali: A machine learning potential for biological and organic chemistry with semi-empirical cost and DFT accuracy. *J. Chem. Phys* **2021**, *155*.
- (27) Thölke, P.; De Fabritiis, G. Equivariant transformers for neural network based molecular potentials. International Conference on Learning Representations. 2022.

- (28) Batatia, I.; Kovacs, D. P.; Simm, G.; Ortner, C.; Csányi, G. MACE: Higher order equivariant message passing neural networks for fast and accurate force fields. *Advances in Neural Information Processing Systems* **2022**, *35*, 11423–11436.
- (29) Smith, J. S.; Isayev, O.; Roitberg, A. E. ANI-1: an extensible neural network potential with DFT accuracy at force field computational cost. *Chem. Sci* **2017**, *8*, 3192–3203.
- (30) Smith, J. S.; Nebgen, B.; Lubbers, N.; Isayev, O.; Roitberg, A. E. Less is more: Sampling chemical space with active learning. *J. Chem. Phys* **2018**, *148*, 241733.
- (31) Smith, J. S.; Nebgen, B. T.; Zubatyuk, R.; Lubbers, N.; Devereux, C.; Barros, K.; Tretiak, S.; Isayev, O.; Roitberg, A. E. Approaching coupled cluster accuracy with a general-purpose neural network potential through transfer learning. *Nat. Commun* **2019**, *10*, 1–8.
- (32) Stevenson, J. M.; Jacobson, L. D.; Zhao, Y.; Wu, C.; Maple, J.; Leswing, K.; Harder, E.; Abel, R. Schrödinger-ANI: An Eight-Element Neural Network Interaction Potential with Greatly Expanded Coverage of Druglike Chemical Space. *arXiv preprint arXiv:1912.05079* **2019**,
- (33) Devereux, C.; Smith, J. S.; Davis, K. K.; Barros, K.; Zubatyuk, R.; Isayev, O.; Roitberg, A. E. Extending the Applicability of the ANI Deep Learning Molecular Potential to Sulfur and Halogens. *J. Chem. Theory Comput* **2020**, *16*, 4192–4202.
- (34) Behler, J.; Parrinello, M. Generalized neural-network representation of high-dimensional potential-energy surfaces. *Phys. Rev. Lett* **2007**, *98*, 146401.
- (35) Vanommeslaeghe, K.; Hatcher, E.; Acharya, C.; Kundu, S.; Zhong, S.; Shim, J.; Darian, E.; Guvench, O.; Lopes, P.; Vorobyov, I.; MacKerell Jr, A. D. CHARMM general force field: A force field for drug-like molecules compatible with the CHARMM all-atom additive biological force fields. *J. Comput. Chem* **2010**, *31*, 671–690.

- (36) Vanommeslaeghe, K.; Raman, E. P.; MacKerell Jr, A. D. Automation of the CHARMM General Force Field (CGenFF) II: assignment of bonded parameters and partial atomic charges. *J. Chem. Inf. Model* **2012**, *52*, 3155–3168.
- (37) Wang, J.; Wolf, R. M.; Caldwell, J. W.; Kollman, P. A.; Case, D. A. Development and testing of a general amber force field. *J. Comput. Chem* **2004**, *25*, 1157–1174.
- (38) Jorgensen, W. L.; Tirado-Rives, J. Potential energy functions for atomic-level simulations of water and organic and biomolecular systems. *Proc. Natl. Acad. Sci* **2005**, *102*, 6665–6670.
- (39) Mobley, D. L.; Bannan, C. C.; Rizzi, A.; Bayly, C. I.; Chodera, J. D.; Lim, V. T.; Lim, N. M.; Beauchamp, K. A.; Slochower, D. R.; Shirts, M. R.; Gilson, M. K.; Eastman, P. K. Escaping atom types in force fields using direct chemical perception. *J. Chem. Theory Comput* **2018**, *14*, 6076–6092.
- (40) Lahey, S.-L. J.; Thien Phuc, T. N.; Rowley, C. N. Benchmarking Force Field and the ANI Neural Network Potentials for the Torsional Potential Energy Surface of Biaryl Drug Fragments. *J. Chem. Inf. Model* **2020**,
- (41) Lahey, S.-L. J.; Rowley, C. N. Simulating protein–ligand binding with neural network potentials. *Chem. Sci* **2020**, *11*, 2362–2368.
- (42) Warshel, A.; Levitt, M. Theoretical studies of enzymic reactions: dielectric, electrostatic and steric stabilization of the carbonium ion in the reaction of lysozyme. *J. Mol. Biol* **1976**, *103*, 227–249.
- (43) Lin, H.; Truhlar, D. G. QM/MM: what have we learned, where are we, and where do we go from here? *Theor. Chem. Acc* **2007**, *117*, 185–199.
- (44) Senn, H. M.; Thiel, W. QM/MM methods for biomolecular systems. *Angew. Chem* **2009**, *48*, 1198–1229.

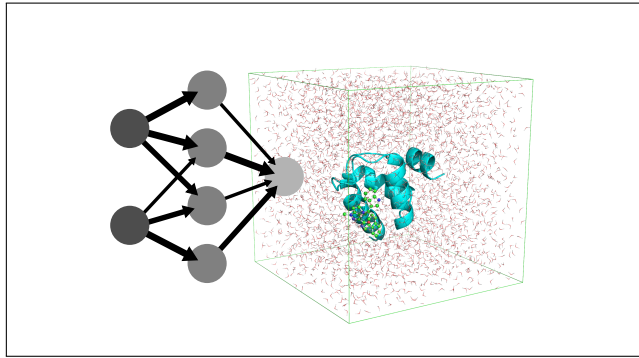
- (45) Rufa, D. A.; Macdonald, H. E. B.; Fass, J.; Wieder, M.; Grinaway, P. B.; Roitberg, A. E.; Isayev, O.; Chodera, J. D. Towards chemical accuracy for alchemical free energy calculations with hybrid physics-based machine learning/molecular mechanics potentials. *BioRxiv* **2020**,
- (46) Wang, L.; Wu, Y.; Deng, Y.; Kim, B.; Pierce, L.; Krilov, G.; Lupyan, D.; Robinson, S.; Dahlgren, M. K.; Greenwood, J.; Romero, D. L.; Masse, C.; Knight, J. L.; Steinbrecher, T.; Beuming, T.; Damm, W.; Harder, E.; Sherman, W.; Brewer, M.; Wester, R.; Murcko, M.; Frye, L.; Farid, R.; Lin, T.; Mobley, D. L.; Jorgensen, W. L.; Berne, B. J.; Friesner, R. A.; Abel, R. Accurate and reliable prediction of relative ligand binding potency in prospective drug discovery by way of a modern free-energy calculation protocol and force field. *J. Am. Chem. Soc* **2015**, *137*, 2695–2703.
- (47) Vant, J. W.; Lahey, S.-L. J.; Jana, K.; Shekhar, M.; Sarkar, D.; Munk, B. H.; Kleinekathöfer, U.; Mittal, S.; Rowley, C.; Singharoy, A. Flexible Fitting of Small Molecules into Electron Microscopy Maps Using Molecular Dynamics Simulations with Neural Network Potentials. *J. Chem. Inf. Model* **2020**,
- (48) Xu, M.; Zhu, T.; Zhang, J. Z. Automatically Constructed Neural Network Potentials for Molecular Dynamics Simulation of Zinc Proteins. *Front. Chem* **2021**, *9*.
- (49) Paszke, A.; Gross, S.; Massa, F.; Lerer, A.; Bradbury, J.; Chanan, G.; Killeen, T.; Lin, Z.; Gimelshein, N.; Antiga, L.; Desmaison, A.; Köpf, A.; Yang, E.; DeVito, Z.; Raison, M.; Tejani, A.; Chilamkurthy, S.; Steiner, B.; Fang, L.; Bai, J.; Chintala, S. Pytorch: An imperative style, high-performance deep learning library. *Advances in neural information processing systems* **2019**, *32*.
- (50) Barducci, A.; Bonomi, M.; Parrinello, M. Metadynamics. *Wiley Interdiscip. Rev.: Comput. Mol. Sci* **2011**, *1*, 826–843.
- (51) Eastman, P.; Swails, J.; Chodera, J. D.; McGibbon, R. T.; Zhao, Y.; Beauchamp, K. A.;

- Wang, L.-P.; Simmonett, A. C.; Harrigan, M. P.; Stern, C. D.; Wiewiora, R. P.; Brooks, B. R.; Pande, V. S. OpenMM 7: Rapid development of high performance algorithms for molecular dynamics. *PLoS Comput. Biol* **2017**, *13*, e1005659.
- (52) Eastman, P. OpenMM-Torch. <https://github.com/openmm/openmm-torch>, 2021; accessed 2023/05/21.
- (53) Gao, X.; Ramezanghorbani, F.; Isayev, O.; Smith, J. S.; Roitberg, A. E. TorchANI: A free and open source PyTorch-based deep learning implementation of the ANI neural network potentials. *J. Chem. Inf. Model* **2020**, *60*, 3408–3415.
- (54) Eastman, P.; Galvelis, R. NNPOps. <https://github.com/openmm/nnpops>, 2021; accessed 2023/05/21.
- (55) TorchMD-NET. <https://github.com/torchmd/torchmd-net>, accessed 2023/05/21.
- (56) Barducci, A.; Bussi, G.; Parrinello, M. Well-tempered metadynamics: a smoothly converging and tunable free-energy method. *Phys. Rev. Lett* **2008**, *100*, 020603.
- (57) Tribello, G. A.; Bonomi, M.; Branduardi, D.; Camilloni, C.; Bussi, G. PLUMED 2: New feathers for an old bird. *Comput. Phys. Commun* **2014**, *185*, 604–613.
- (58) Wang, R.; Fang, X.; Lu, Y.; Wang, S. The PDBbind database: Collection of binding affinities for protein–ligand complexes with known three-dimensional structures. *J. Med. Chem* **2004**, *47*, 2977–2980.
- (59) Liu, Z.; Su, M.; Han, L.; Liu, J.; Yang, Q.; Li, Y.; Wang, R. Forging the basis for developing protein–ligand interaction scoring functions. *Acc. Chem. Res* **2017**, *50*, 302–309.
- (60) Bäckbro, K.; Löwgren, S.; Österlund, K.; Atepo, J.; Unge, T.; Hultén, J.; Bonham, N. M.; Schaal, W.; Karlén, A.; Hallberg, A. Unexpected binding mode of a cyclic sulfamide HIV-1 protease inhibitor. *J. Med. Chem* **1997**, *40*, 898–902.

- (61) Skulnick, H. I.; Johnson, P. D.; Aristoff, P. A.; Morris, J. K.; Lovasz, K. D.; Howe, W. J.; Watenpaugh, K. D.; Janakiraman, M. N.; Anderson, D. J.; Reischer, R. J.; Schwartz, T. M.; Banitt, L. S.; Tomich, P. K.; Lynn, J. C.; Horng, M.-M.; Chong, K.-T.; Hinshaw, R. R.; Dolak, L. A.; Seest, E. P.; Schwende, F. J.; Rush, B. D.; Howard, G. M.; Toth, L. N.; Wilkinson, K. R.; Kakuk, T. J.; Johnson, C. W.; Cole, S. L.; Zaya, R. M.; Zipp, G. L.; Possert, P. L.; Dalga, R. J.; Zhong, W.-Z.; Williams, M. G.; Romines, K. R. Structure-based design of nonpeptidic HIV protease inhibitors: the sulfonamide-substituted cyclooctylpyranones. *J. Med. Chem* **1997**, *40*, 1149–1164.
- (62) Qiao, J. X.; Chang, C.-H.; Cheney, D. L.; Morin, P. E.; Wang, G. Z.; King, S. R.; Wang, T. C.; Rendina, A. R.; Luetzgen, J. M.; Knabb, R. M.; Wexler, R. R.; Lam, P. Y. SAR and X-ray structures of enantiopure 1, 2-cis-(1R, 2S)-cyclopentylidiamine and cyclohexylidiamine derivatives as inhibitors of coagulation Factor Xa. *Bioorg. Med. Chem. Lett* **2007**, *17*, 4419–4427.
- (63) Nie, Z.; Perretta, C.; Erickson, P.; Margosiak, S.; Lu, J.; Averill, A.; Almasy, R.; Chu, S. Structure-based design and synthesis of novel macrocyclic pyrazolo [1, 5-a][1, 3, 5] triazine compounds as potent inhibitors of protein kinase CK2 and their anticancer activities. *Bioorg. Med. Chem. Lett* **2008**, *18*, 619–623.
- (64) Doerr, S.; Harvey, M.; Noé, F.; De Fabritiis, G. HTMD: high-throughput molecular dynamics for molecular discovery. *J. Chem. Theory Comput* **2016**, *12*, 1845–1852.
- (65) Smith, J. S.; Isayev, O.; Roitberg, A. E. ANI-1, A data set of 20 million calculated off-equilibrium conformations for organic molecules. *Sci. Data* **2017**, *4*, 1–8.
- (66) Conda. <https://docs.conda.io/>, accessed 2023/05/21.
- (67) conda-forge. <https://conda-forge.org/>, accessed 2023/05/21.
- (68) HTMD documentation. <https://software.acellera.com/htmd>, accessed 2023/05/21.

- (69) ACEMD documentation. <https://software.acellera.com/acemd>, accessed 2023/05/21.
- (70) Sugita, Y.; Okamoto, Y. Replica-exchange molecular dynamics method for protein folding. *Chem. Phys. Lett* **1999**, *314*, 141–151.
- (71) Izrailev, S.; Stepaniants, S.; Isralewitz, B.; Kosztin, D.; Lu, H.; Molnar, F.; Wriggers, W.; Schulten, K. Steered molecular dynamics. *Computational Molecular Dynamics: Challenges, Methods, Ideas: Proceedings of the 2nd International Symposium on Algorithms for Macromolecular Modelling*, Berlin, May 21–24, 1997. 1999; pp 39–65.

TOC Graphic



SUPPLEMENTARY INFORMATION: NNP/MM: Accelerating molecular dynamics simulations with machine learning potentials and molecular mechanics

Raimondas Galvelis,^{*,†} Alejandro Varela-Rial,^{‡,¶} Stefan Doerr,[‡] Roberto Fino,[†]
Peter Eastman,[§] Thomas E. Markland,[§] John D. Chodera,^{||} and Gianni De
Fabritiis^{*,†,¶,⊥}

[†]*Acellera Labs, C/ Doctor Trueta 183, 08005 Barcelona, Spain*

[‡]*Acellera Ltd, Devonshire House 582, HA7 1JS, United Kingdom*

[¶]*Computational Science Laboratory, Universitat Pompeu Fabra, PRBB, C/ Doctor
Aiguader 88, 08003 Barcelona, Spain*

[§]*Department of Chemistry, Stanford University, 337 Campus Drive, Stanford, CA, 94305,
USA*

^{||}*Computational and Systems Biology Program, Sloan Kettering Institute, Memorial Sloan
Kettering Cancer Center, New York, NY 10065, USA*

[⊥]*Institució Catalana de Recerca i Estudis Avançats (ICREA), Passeig Lluís Companys 23,
08010 Barcelona, Spain*

E-mail: r.galvelis@acellera.com; g.defabritiis@gmail.com

Preparation and simulation conditions for the fragment system

The system preparation has been carried out with HTMD.[?] The fragment is constructed from SMILES and solvated with 5 Å padding.

The molecular topology and FF parameters files have been prepared with HTMD.[?] The force field parameters are obtained with GAFF2[?] or modeled with ANI-2x[?] depending on the simulation method. For water, the rigid TIP3P[?] model is used. The bonds between hydrogens and heavy atoms (H–X) are constrained and the hydrogen masses are repartitioned to 4.0 u. The electrostatic interactions are computed with PME[?] and the van der Waals interactions with the cutoff of 9.0 Å. The MD time step for the MM simulations is 4.0 fs, but for NNP/MM it is reduced to 2.0 fs due to stability issues. The temperature and pressures are maintained with the Langevin thermostat (the damping constant of 0.1 ps⁻¹) and the isotropic Monte Carlo barostat, respectively.

For metadynamics (MTD), PLUMED[?] plugin is used. Two dihedral angles are used as collective variables. The bias potential is updated every 1 ps, kernel height is 4.185 kcal/mol and width 10 deg. The bias factor is set to 5 (i.e. the effective temperature is 1550 K).[?]

Each protein-ligand complex has been equilibrated with the following procedure. First, the system is minimized for 500 steps. Second, the system is equilibrated for 1.0 ns with the NPT ensemble (T = 310 K and P = 1.0 bar). For the production simulations, the NVT ensemble (T = 310 K) is used without any restraints. Simulation trajectories are saved every 50 ps.

Dihedral angle series of the fragment

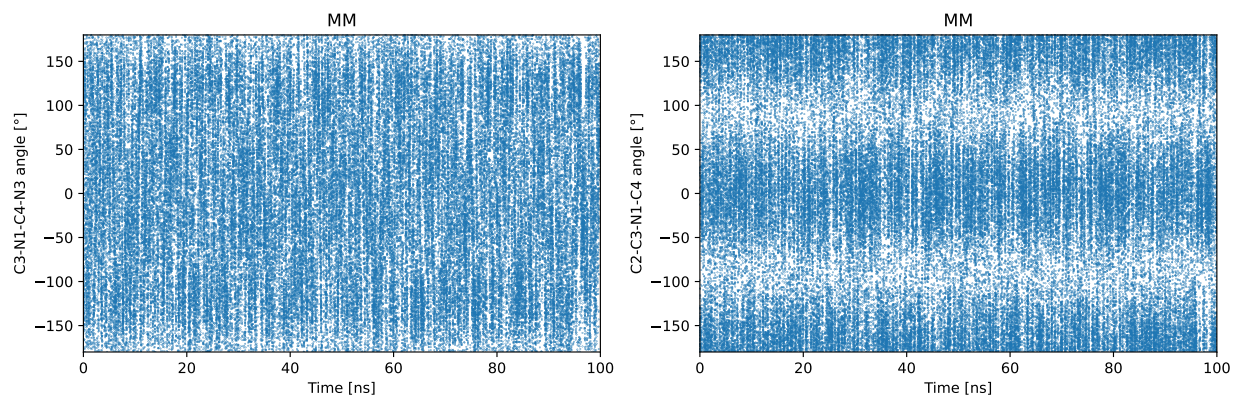


Figure S1: The dihedral angle series of the fragment from the MM simulation.

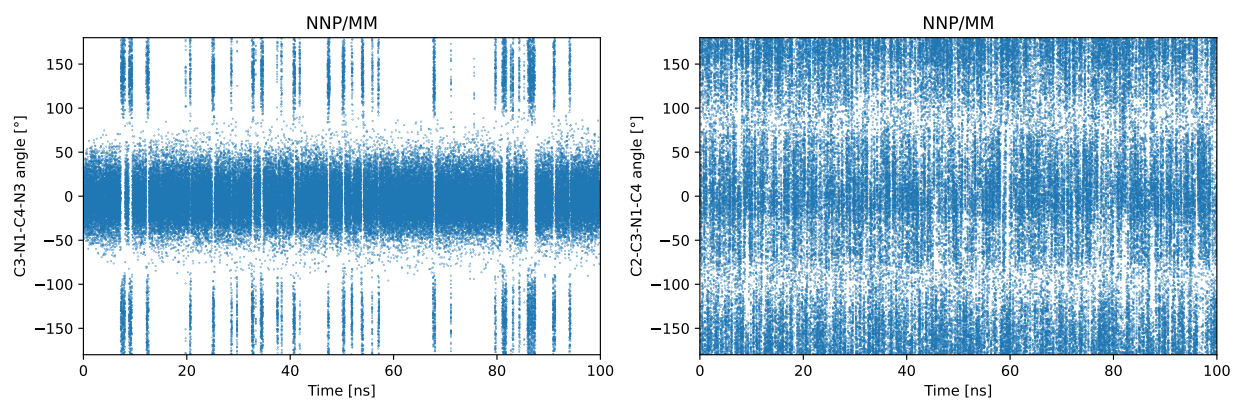


Figure S2: The dihedral angle series of the fragment from the NNP/MM simulation.

Preparation and simulation conditions for protein-ligand systems

The system preparation has been carried out with HTMD.[?] First, the structure of a protein-ligand complex is downloaded from the PDB[?] database. Only the protein and ligand are kept, and the other atoms are removed. Second, the protein is protonated at pH = 7.0 with PROPKA[?] and its hydrogen bonds are optimized with PDB2PQR.[?] Finally, the system is solvated with 5 Å padding and neutralized with Na⁺ or Cl⁻ ions.

The molecular topology and FF parameters files have been prepared with HTMD.[?] For the protein, AMBER ff14SB[?] FF is used. For the ligand, the force field parameters are obtained with GAFF2[?] or modeled with ANI-2x[?] depending on the simulation method. For water, the rigid TIP3P[?] model is used. The bonds between hydrogens and heavy atoms (H-X) are constrained and the hydrogen masses are repartitioned to 4.0 u. The electrostatic interactions are computed with PME[?] and the van der Waals interactions with the cutoff of 9.0 Å. The MD time step for the MM simulations is 4.0 fs, but for NNP/MM it is reduced to 2.0 fs due to stability issues. The temperature and pressures are maintained with the Langevin thermostat (the damping constant of 0.1 ps⁻¹) and the isotropic Monte Carlo barostat, respectively.

Each protein-ligand complex has been equilibrated with the following procedure. First, the system is minimized for 500 steps with the harmonic positional restraint applied to the protein (the force constant for backbone atoms is 1.0 kcal/mol/Å² and the one for the side-chain atoms is 1.0 kcal/mol/Å²). Second, the system is equilibrated for 1.0 ns with the NPT ensemble (T = 310 K and P = 1.0 bar). The force constants of the restraints are reduced linearly to 1.0 kcal/mol/Å² during the first 0.5 ns of the simulation. For the production simulations, the NVT ensemble (T = 310 K) is used without any restraints. Simulation trajectories are saved every 50 ps.

Dihedral angle scans

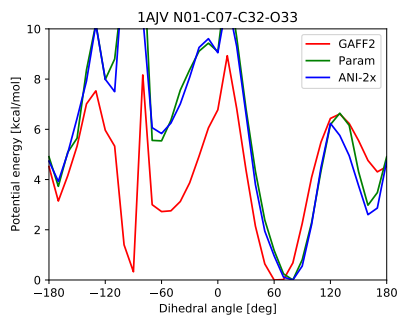


Figure S3: Energy profile of the dihedral angle N01-C07-C32-O33 scan of 1AJV ligand. Rotamer energies are computed with different methods.

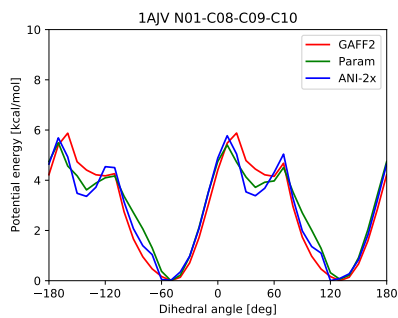


Figure S4: Energy profile of the dihedral angle N01-C08-C09-C10 scan of 1AJV ligand. Rotamer energies are computed with different methods.

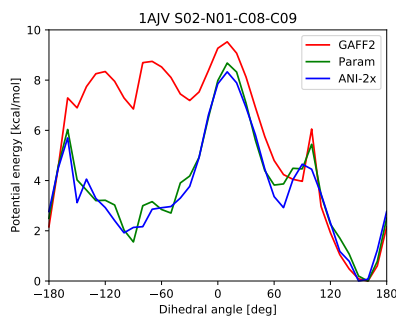


Figure S5: Energy profile of the dihedral angle S02-N01-C08-C09 scan of 1AJV ligand. Rotamer energies are computed with different methods.

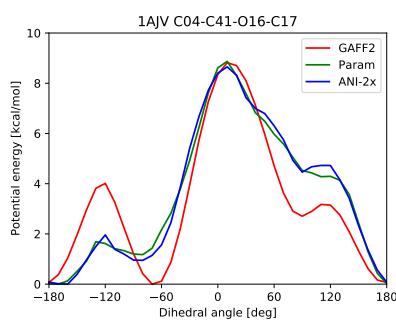


Figure S6: Energy profile of the dihedral angle C04-C41-O16-C17 scan of 1AJV ligand. Rotamer energies are computed with different methods.

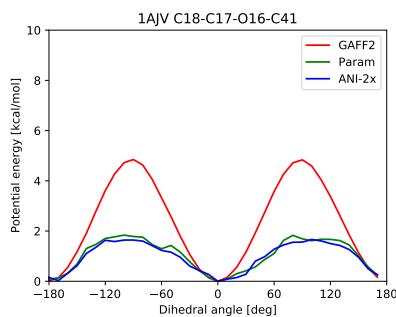


Figure S7: Energy profile of the dihedral angle C18-C17-O16-C41 scan of 1AJV ligand. Rotamer energies are computed with different methods.

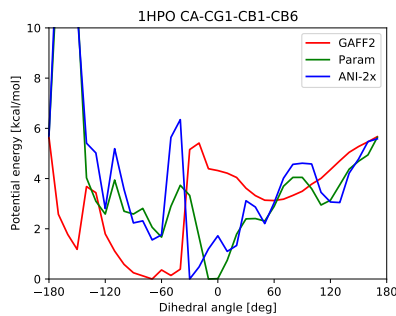


Figure S8: Energy profile of the dihedral angle CA-CG1-CB1-CB6 scan of 1HPO ligand. Rotamer energies are computed with different methods.

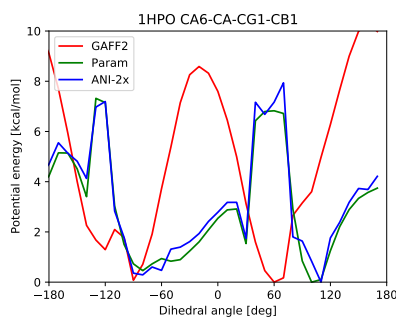


Figure S9: Energy profile of the dihedral angle CA6-CA-CG1-CB1 scan of 1HPO ligand. Rotamer energies are computed with different methods.

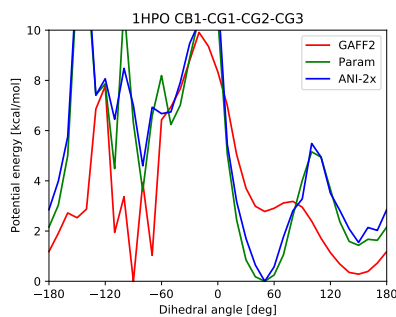


Figure S10: Energy profile of the dihedral angle CB1-CG1-CG2-CG3 scan of 1HPO ligand. Rotamer energies are computed with different methods.

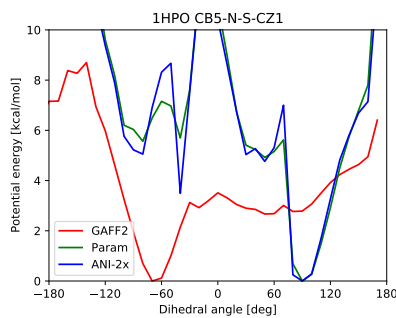


Figure S11: Energy profile of the dihedral angle CB5-N-S-CZ1 scan of 1HPO ligand. Rotamer energies are computed with different methods.

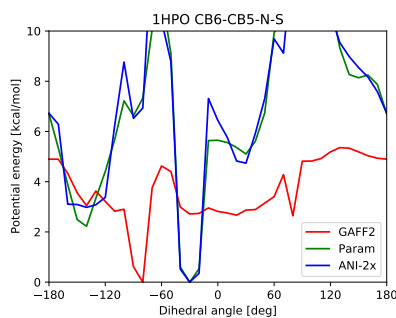


Figure S12: Energy profile of the dihedral angle CB6-CB5-N-S scan of 1HPO ligand. Rotamer energies are computed with different methods.

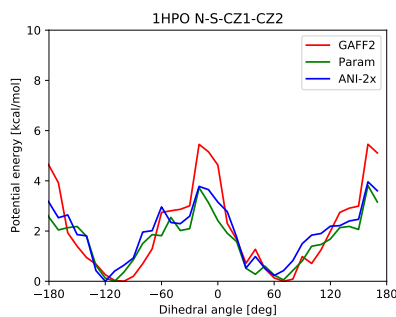


Figure S13: Energy profile of the dihedral angle N-S-CZ1-CZ2 scan of 1HPO ligand. Rotamer energies are computed with different methods.

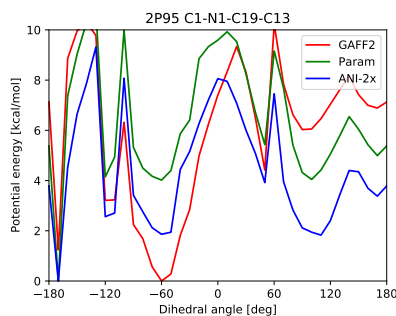


Figure S14: Energy profile of the dihedral angle C1-N1-C19-C13 scan of 2P95 ligand. Rotamer energies are computed with different methods.

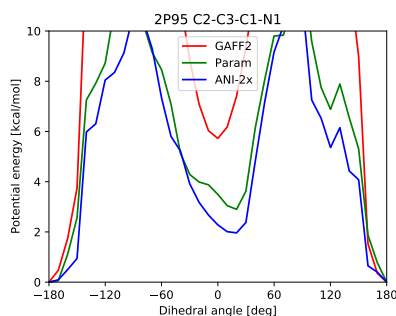


Figure S15: Energy profile of the dihedral angle C2-C3-C1-N1 scan of 2P95 ligand. Rotamer energies are computed with different methods.

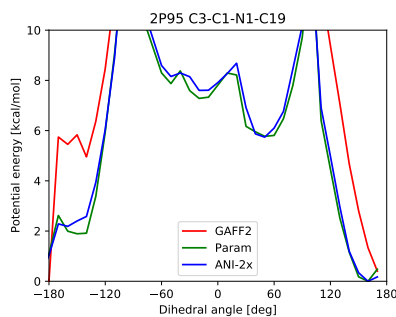


Figure S16: Energy profile of the dihedral angle C3-C1-N1-C19 scan of 2P95 ligand. Rotamer energies are computed with different methods.

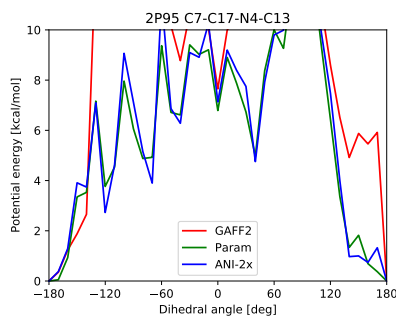


Figure S17: Energy profile of the dihedral angle C7-C17-N4-C13 scan of 2P95 ligand. Rotamer energies are computed with different methods.

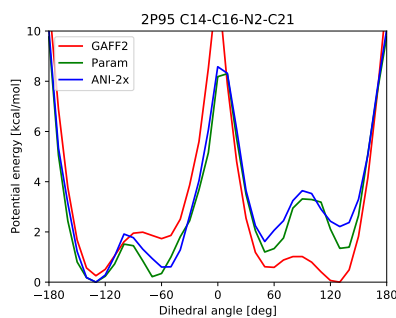


Figure S18: Energy profile of the dihedral angle C14-C16-N2-C21 scan of 2P95 ligand. Rotamer energies are computed with different methods.

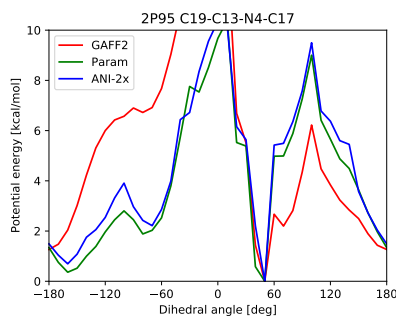


Figure S19: Energy profile of the dihedral angle C19-C13-N4-C17 scan of 2P95 ligand. Rotamer energies are computed with different methods.

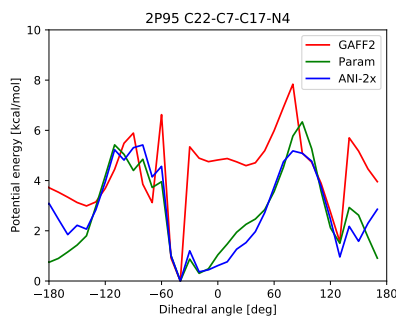


Figure S20: Energy profile of the dihedral angle C22-C7-C17-N4 scan of 2P95 ligand. Rotamer energies are computed with different methods.

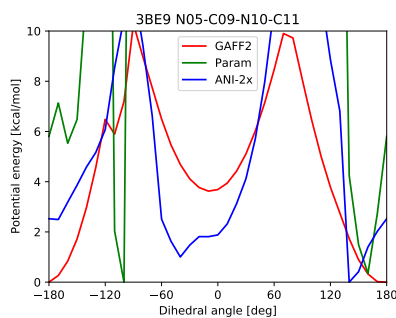


Figure S21: Energy profile of the dihedral angle N05-C09-N10-C11 scan of 3BE9 ligand. Rotamer energies are computed with different methods.

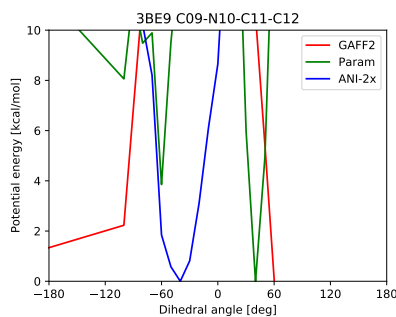


Figure S22: Energy profile of the dihedral angle C09-N10-C11-C12 scan of 3BE9 ligand. Rotamer energies are computed with different methods.

Time series of protein RMSD

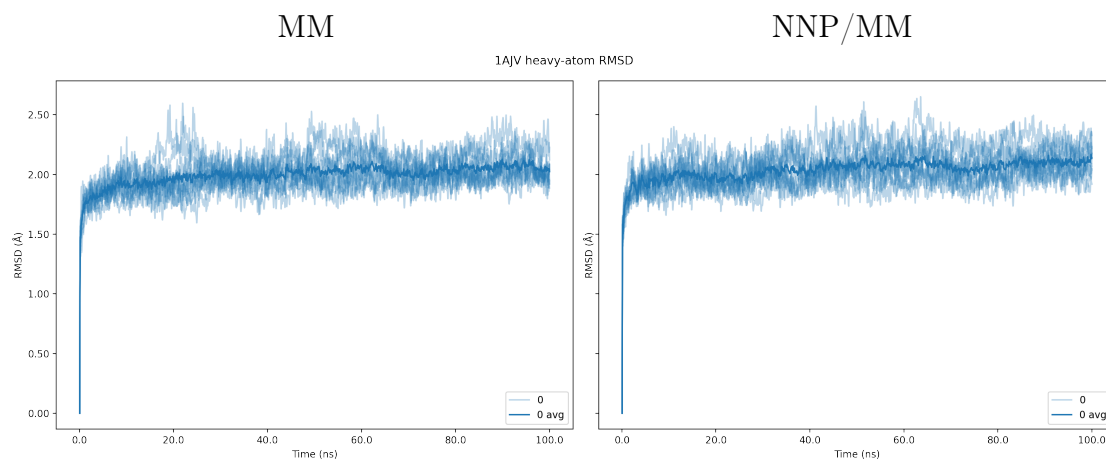


Figure S23: Time series of protein RMSD for 1AJV with the different methods (MM and NNP/MM). The independent simulations are colored in light blue and the average is in dark blue.

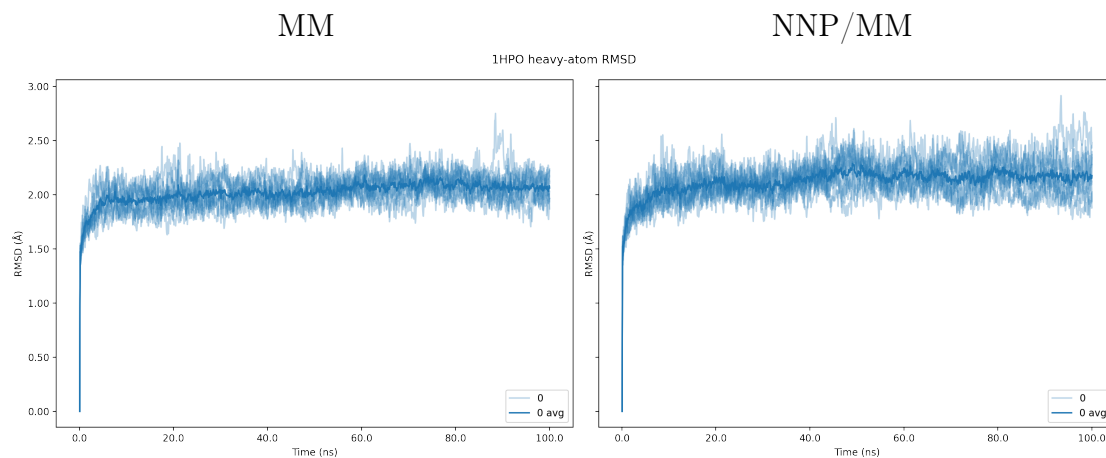


Figure S24: Time series of protein RMSD for 1HPO with the different methods (MM and NNP/MM). The independent simulations are colored in light blue and the average is in dark blue.

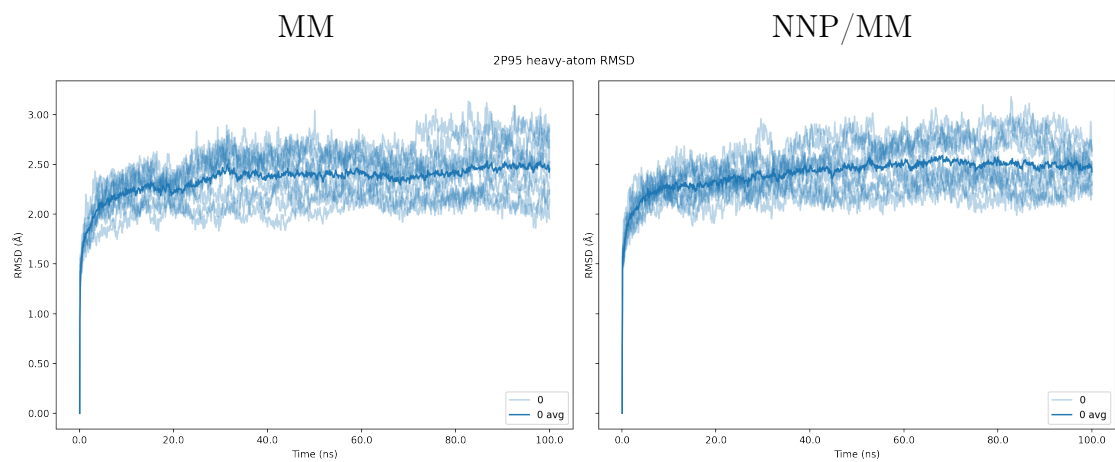


Figure S25: Time series of protein RMSD for 2P95 with the different methods (MM and NNP/MM). The independent simulations are colored in light blue and the average is in dark blue.

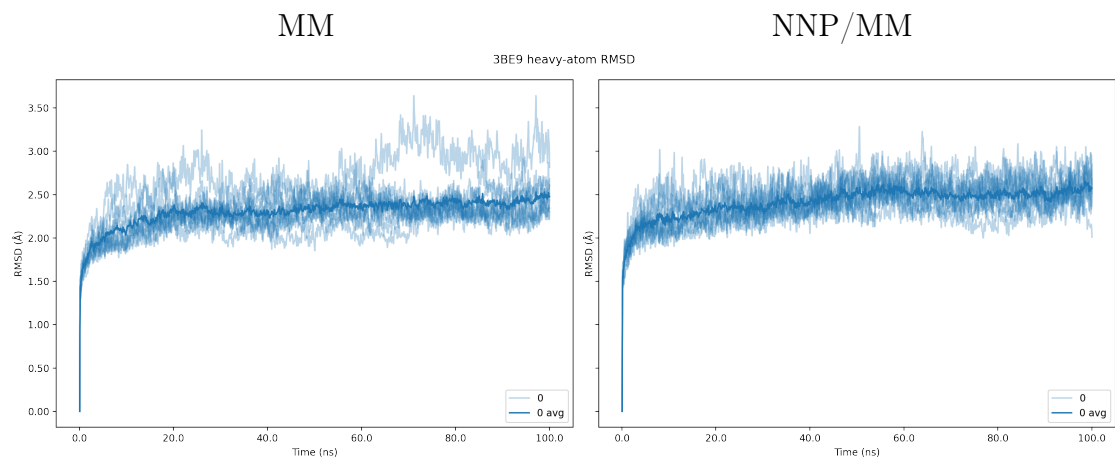


Figure S26: Time series of protein RMSD for 3BE9 with the different methods (MM and NNP/MM). The independent simulations are colored in light blue and the average is in dark blue.

Per-residue RMSF of protein

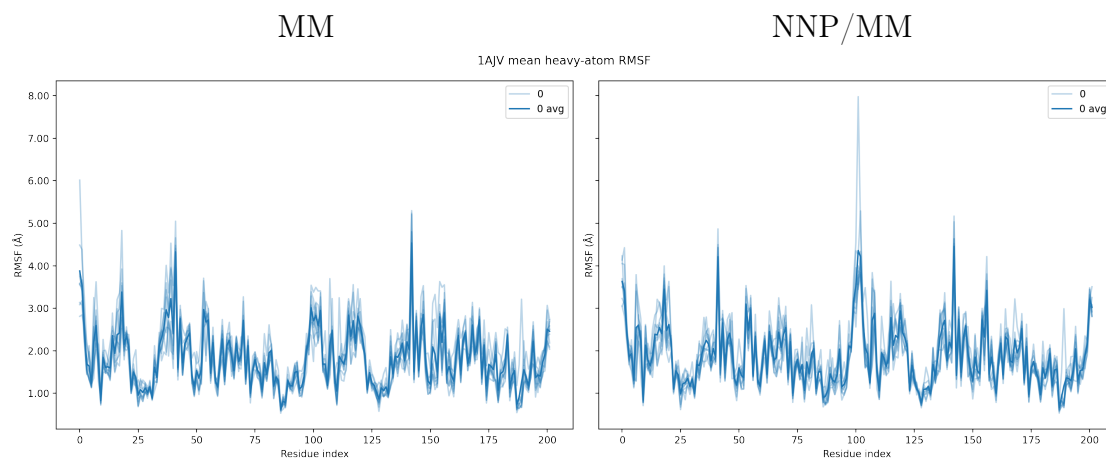


Figure S27: Residue RMSF of protein for 1AJV with the different methods (MM and NNP/MM). The independent simulations are colored in light blue and the average is in dark blue.

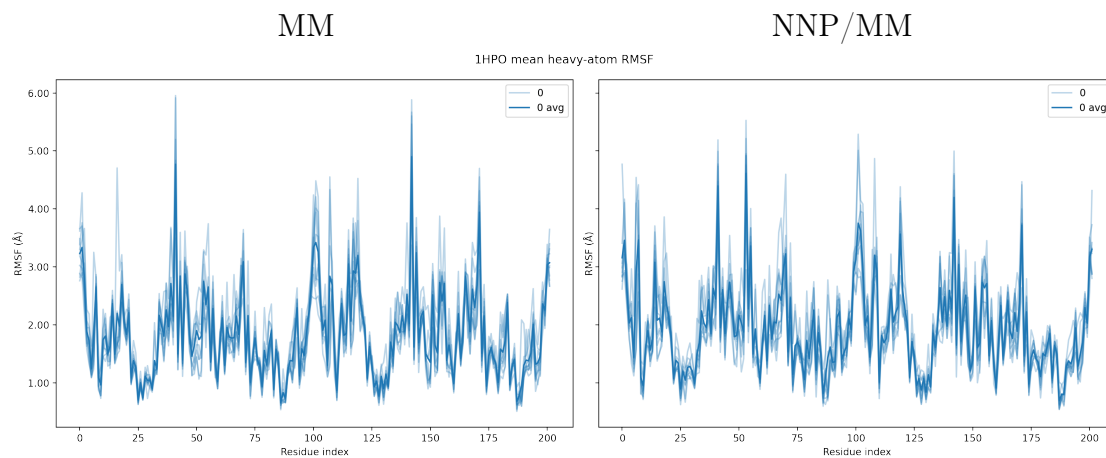


Figure S28: Residue RMSF of protein for 1HPO with the different methods (MM and NNP/MM). The independent simulations are colored in light blue and the average is in dark blue.

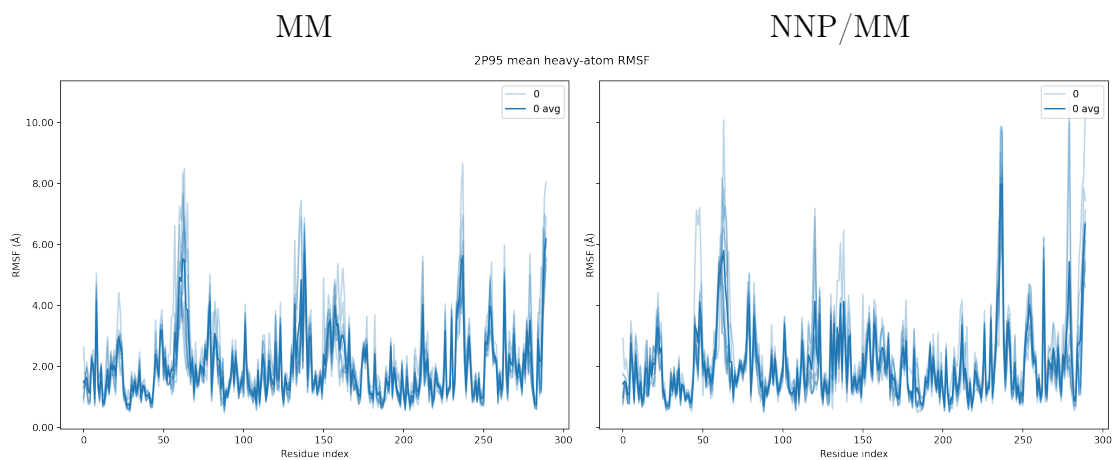


Figure S29: Residue RMSF of protein for 2P95 with the different methods (MM and NNP/MM). The independent simulations are colored in light blue and the average is in dark blue.

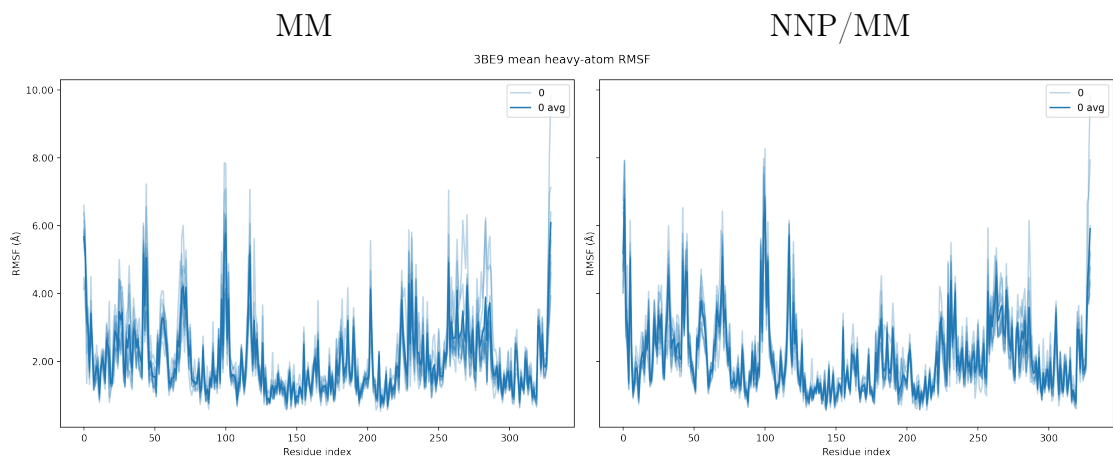


Figure S30: Residue RMSF of protein for 3BE9 with the different methods (MM and NNP/MM). The independent simulations are colored in light blue and the average is in dark blue.

Time series of ligand RMSD

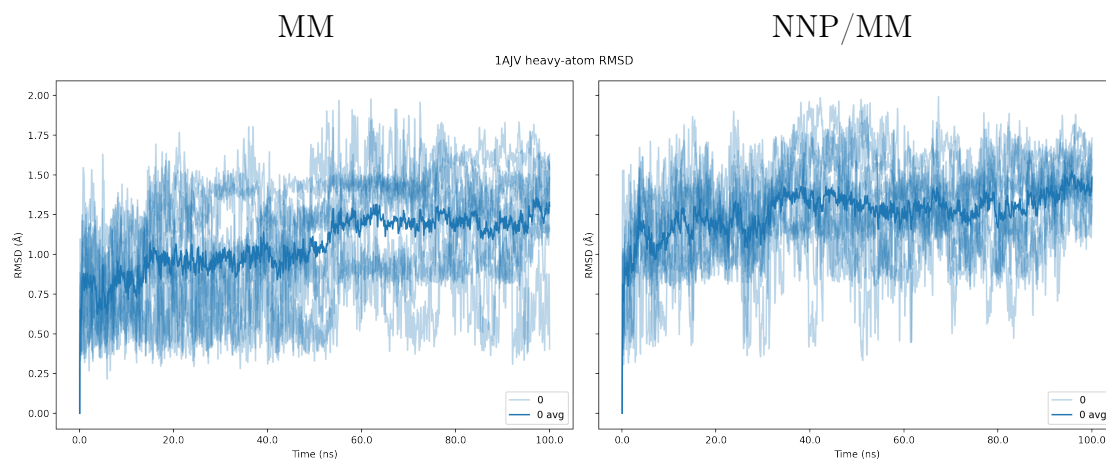


Figure S31: Time series of ligand RMSD for 1AJV with the different methods (MM and NNP/MM). The independent simulations are colored in light blue and the average is in dark blue.

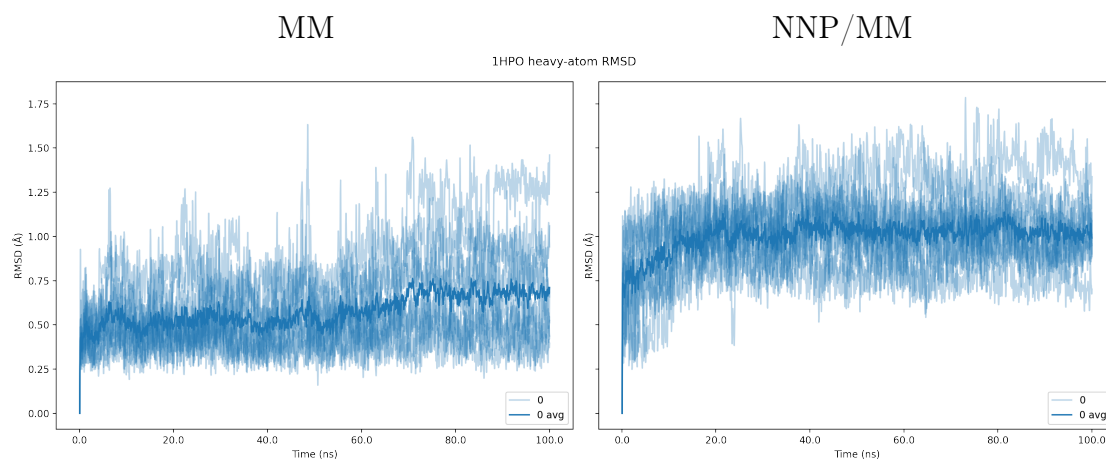


Figure S32: Time series of ligand RMSD for 1HPO with the different methods (MM and NNP/MM). The independent simulations are colored in light blue and the average is in dark blue.

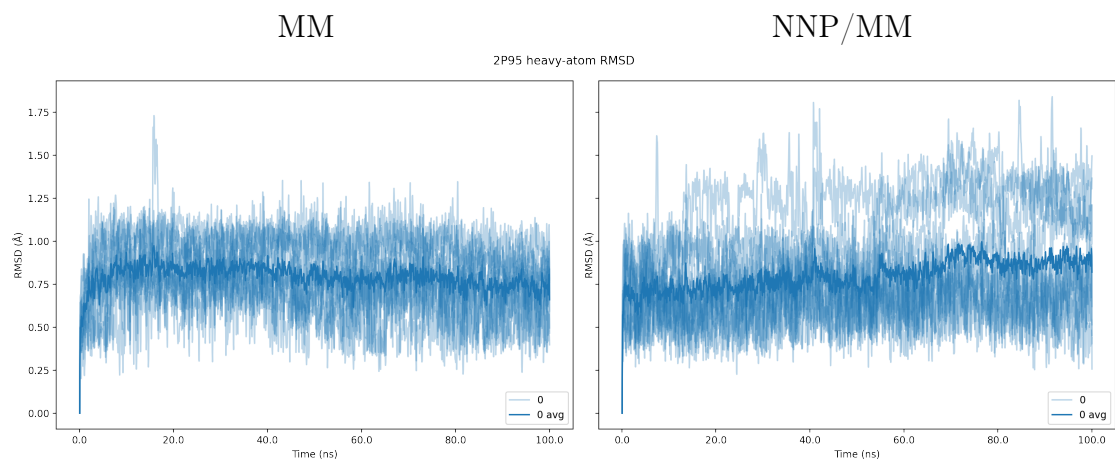


Figure S33: Time series of ligand RMSD for 2P95 with the different methods (MM and NNP/MM). The independent simulations are colored in light blue and the average is in dark blue.

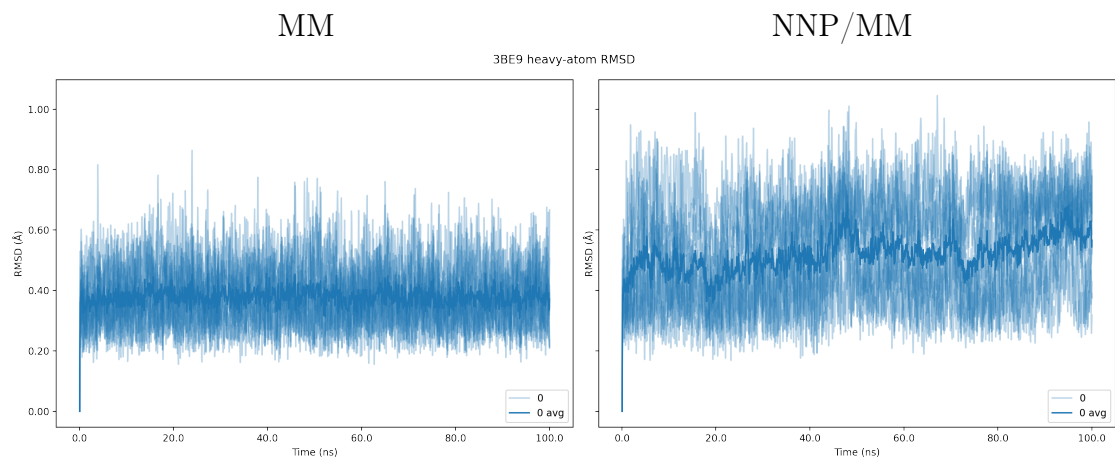


Figure S34: Time series of ligand RMSD for 3BE9 with the different methods (MM and NNP/MM). The independent simulations are colored in light blue and the average is in dark blue.

Protein-ligand interactions

Protein-ligand interactions have been detected following criteria:

- H-bond: the donor and acceptor distance (D–A) is $<2.5 \text{ \AA}$ and the D–H–A angle is $>120^\circ$.
- π - π : the distance between the centers of aromatic rings (R–R) and the angle between their norms (N) satisfying one of these criteria:
 - R–R is $<4.4 \text{ \AA}$ and N is $<30^\circ$.
 - R–R is $<5.5 \text{ \AA}$ and N is $>60^\circ$.
- Cation- π : the distance between a positively-charged atom (P) and the center of the aromatic ring (R) is $<5.0 \text{ \AA}$ and the angle of P–R with respect to the plane of R is $>60^\circ$.
- σ -hole: the distance between halogen atom (H) and the center of the aromatic ring (R) is $<4.0 \text{ \AA}$ and the angle of H–R with respect to the plane of R is $>60^\circ$.

The trajectories have been sampled every 50 ps and the probabilities computed aggregating data from all the 10 independent simulations.

Table S1: Probability of 1AJV protein-ligand interactions in the MM simulations. The interactions with a lower probability than 0.01 are excluded.

Interaction	Residue	Probability
H-bond	ASP:26	0.87665
H-bond	ASP:26	0.99235
H-bond	ILE:51	0.96835
H-bond	ASH:127	0.26010
H-bond	ASH:127	0.51815
H-bond	ILE:152	0.88880

Table S2: Probability of 1AJV protein-ligand interactions in the NNP/MM simulations. The interactions with a lower probability than 0.01 are excluded.

Interaction	Residue	Probability
H-bond	ASP:26	0.99210
H-bond	ASP:26	0.99140
H-bond	ILE:51	0.96035
H-bond	ASH:127	0.05240
H-bond	ASH:127	0.11475
H-bond	ILE:152	0.91555

Table S3: Probability of 1HPO protein-ligand interactions in the MM simulations. The interactions with a lower probability than 0.01 are excluded.

Interaction	Residue	Probability
Cation- π	ARG:9	0.43165
H-bond	ASH:26	0.11160
H-bond	ILE:51	0.36980
H-bond	ILE:51	0.02740
H-bond	ASP:127	0.94340
H-bond	ASP:131	0.28660
H-bond	GLY:150	0.92555
H-bond	GLY:150	0.57730
H-bond	GLY:151	0.01885
H-bond	ILE:152	0.90360

Table S4: Probability of 1HPO protein-ligand interactions in the NNP/MM simulations. The interactions with a lower probability than 0.01 are excluded.

Interaction	Residue	Probability
Cation- π	ARG:9	0.76190
H-bond	ASH:26	0.10260
H-bond	ILE:51	0.38165
H-bond	ILE:51	0.10210
H-bond	ASP:127	0.99580
H-bond	ASP:131	0.81165
H-bond	ASP:132	0.01970
H-bond	GLY:150	0.99445
H-bond	GLY:150	0.11820
H-bond	ILE:152	0.89975

Table S5: Probability of 2P95 protein-ligand interactions in the MM simulations. The interactions with a lower probability than 0.01 are excluded.

Interaction	Residue	Probability
π - π	TYR:86	0.62565
π - π	TYR:86	0.10760
π - π	PHE:163	0.03485
π - π	PHE:163	0.57840
π - π	TRP:206	0.56830
H-bond	GLY:207	0.90965
H-bond	GLY:207	0.05580
H-bond	GLY:209	0.35475
σ -hole	TYR:219	0.54095

Table S6: Probability of 2P95 protein-ligand interactions in the NNP/MM simulations. The interactions with a lower probability than 0.01 are excluded.

Interaction	Residue	Probability
π - π	TYR:86	0.63505
π - π	TYR:86	0.08905
π - π	PHE:163	0.06140
π - π	PHE:163	0.59525
π - π	TRP:206	0.01760
π - π	TRP:206	0.64465
H-bond	GLY:207	0.89720
H-bond	GLY:207	0.07225
H-bond	GLY:209	0.54680
σ -hole	TYR:219	0.38280

Table S7: Probability of 3BE9 protein-ligand interactions in the MM simulations. The interactions with a lower probability than 0.01 are excluded.

Interaction	Residue	Probability
H-bond	LYS:64	0.68070
H-bond	VAL:112	0.57070
H-bond	VAL:112	0.38385
π - π	HID:156	0.24210
H-bond	ASP:171	0.26770
H-bond	ASP:171	0.10400

Table S8: Probability of 3BE9 protein-ligand interactions in the NNP/MM simulations. The interactions with a lower probability than 0.01 are excluded.

Interaction	Residue	Probability
H-bond	VAL:41	0.04610
H-bond	LYS:64	0.78265
H-bond	VAL:112	0.65315
H-bond	VAL:112	0.98575
π - π	HID:156	0.24225
H-bond	ASP:171	0.10545
H-bond	ASP:171	0.03135